Characterization of aerodynamic performance of ducted wind turbines: A numerical study

Received: 10 October 2018 | Revised: 14 February 2019 | Accepted: 24 May 2019
DOI: 10.1002/we.2388

WILEY

RESEARCH ARTICLE

Characterization of aerodynamic performance of ducted wind turbines: A numerical study

Vinit V. Dighe | Gael de Oliveira | Francesco Avallone | Gerard J. W. van Bussel

Wind Energy Research Group, Delft University of Technology, Delft, The Netherlands

Correspondence
Vinit V. Dighe, PhD, Researcher, Wind Energy Research Group, Faculty of Aerospace Engineering, Delft University of Technology, Kluyverweg 1, 2629HS Delft, The Netherlands.
Email: V.V.Dighe@tudelft.nl

Funding information
Stichting voor de Technische Wetenschappen, Grant/Award Number: 12728

Abstract

The complex aerodynamic interactions between the rotor and the duct has to be accounted for the design of ducted wind turbines (DWTs). A numerical study to investigate the characteristics of flow around the DWT using a simplified duct–actuator disc (AD) model is carried out. Inviscid and viscous flow calculations are performed to understand the effects of the duct shape and variable AD loadings on the aerodynamic performance coefficients. The analysis shows that the overall aerodynamic performance of the DWT can be increased by increasing the duct cross-sectional camber. Finally, flow fields using viscous calculations are examined to interpret the effects of inner duct wall flow separation on the overall DWT performance.

KEYWORDS

CFD, ducted wind turbines, optimization, panel method, RANS

1 | INTRODUCTION

Ducted wind turbines (DWTs) improve the energy extraction in comparison with horizontal-axis wind turbines (HAWTs).[1] According to van Bussel,[1] the power extraction for a well-designed DWT can exceed the Betz limit by a factor of 2.5. A significant amount of literature on DWT is based on the combined use of theoretical, numerical, and experimental techniques.[2-7] Due to its simplicity and the fact that the results can be obtained analytically, it clearly appears that the classical axial momentum theory (AMT) still remains popular.[8,9] The main limitation of the AMT approach is that the detailed interaction between rotor blade and duct surface is neglected (see Figure 1). As a consequence, the relation between the thrust force exerted on the duct and the rotor is linear. Then, the optimal rotor loading coefficient corresponds to 8/9 despite the presence of the duct.[1] However, in actuality, the thrust force exerted by the duct on the rotor, or vice versa, interact non-linearly.

More recently, numerical studies based on inviscid potential flow theory have been proposed.[10,11] Bontempo and Manna[11] studied the effects of the duct cross section on the performance of DWT using a semianalytical actuator disc (AD) approach. They found that the gain in the performance of the DWT depends upon the aerodynamic duct thrust, which is improved further by increasing the duct profile camber. The inviscid approach offers a substantial cost saving over a full viscous solution, making it a useful tool during the preliminary design stage of DWT. The approach, however, cannot predict the viscous effects on the DWT performance.

Tang et al[12] carried out a detailed experimental investigation on a two-dimensional duct-AD model in order to determine the optimal DWT design. They concluded that the duct wall flow separation could adversely affect the overall DWT performance. Although these experiments did indicate the separation induced losses, the viscous interactions between the duct and the AD was not evaluated. The present paper aims to characterize the aerodynamic performance of DWT based on two-dimensional computational fluid dynamics (CFD) analysis. To this intent, numerical calculations using a panel method and a Reynold-averaged Navier Stokes (RANS) method are shown. The effects of duct cross-sectional camber on the performance coefficients of DWT is investigated. Furthermore, the comparison of the two numerical approaches provide better

ABBREVIATIONS: AD, actuator disc; AMT, axial momentum theory; CFD, computational fluid dynamics; DWT, ducted wind turbine; RANS, Reynolds averaged Navier Stokes equation.

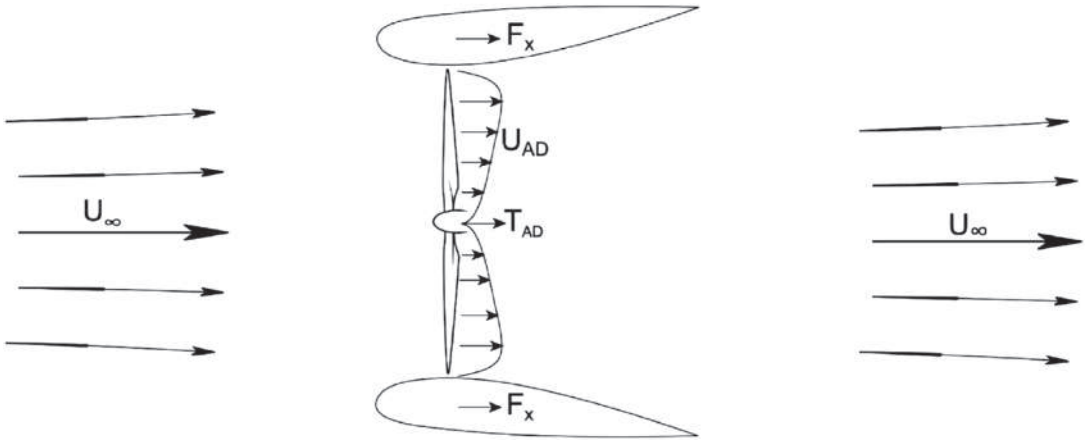

FIGURE 1 Schematic of flow around a ducted wind turbine (DWT)

insights on the importance of the viscous effects and on the limitations of the inviscid flow model for the design of DWT. The rotor is modelled as an AD with radially uniform thrust coefficient. The following section discusses the governing performance coefficients for a duct-AD model. Section 3 describes the computational settings and parameters with a brief description of the numerical methods used. Section 4 explains the verification and validation studies. The duct shape modifications is carried out using the class-shape transformation (CST) method and is discussed in Section 5. Finally, some insights on the performance coefficients with respect to AD loading will be discussed in Section 6, together with flow analysis obtained using RANS simulations.

2 | DUCT-AD FLOW MODEL

The incompressible flow past a turbine is modelled by a flat AD of infinitesimal width. The AD exerts a constant thrust force T_{AD} per unit surface, which corresponds to a nondimensional thrust force coefficient:

$$C_T = \frac{T_{AD}}{\frac{1}{2}\rho U_\infty^2 S_{AD}}, \tag{1}$$

where ρ is the fluid density, U_∞ is the free stream velocity, and S_{AD} is the AD surface area.

For a duct-AD configuration, an additional thrust force F_x, exerted by the duct on the flow, appears. In order to quantify the relative contribution of the duct force F_x on the AD, the duct force coefficient C_x is defined:

$$C_x = \frac{F_x}{\frac{1}{2}\rho U_\infty^2 S_{AD}}. \tag{2}$$

The presence of duct force F_x results in an overall mass flow rate $\dot{\mathbf{m}} = \rho S_{AD} U_{AD}$, when calculated across the AD plane. Although the assumption of constant loading C_T is employed, the free stream velocity computed at the AD plane cannot be regarded as radially uniform, especially for

FIGURE 2 Pictures showing the experimental set-up with hot-wire anemometer placed on the traversing system (left) and pressure taps along the duct surface (right) [Colour figure can be viewed at wileyonlinelibrary.com]

a duct-AD model where the accelerations are higher as compared with a bare AD. In order to account for the non-uniform flow in the radial direction, the mean AD velocity U_{AD} is defined by integrating the differential terms for the local axial velocity U_x across the AD surface:

$$U_{AD} = \frac{1}{S_{AD}} \oint_{S_{AD}} U_x dS, \tag{3}$$

This leads to a power coefficient of the duct-actuator model using AD surface S_{AD} as the reference area:

$$C_P = \frac{P}{\frac{1}{2}\rho U_\infty^3 S_{AD}} = \frac{U_{AD}}{U_\infty} C_T. \tag{4}$$

It is worth mentioning that some studies adopt a different definition for power coefficient in which the reference area is taken at the duct exit section.[11] As a result, the power coefficient obtained is smaller than the one obtained using Equation (4). So that, with the help of reference areas S_{AD} and S_{exit}, the difference in the power coefficients can be expressed as

$$\frac{C_P}{C_{Pexit}} = \frac{S_{AD}}{S_{exit}}. \tag{5}$$

The velocity at the AD U_{AD} and the duct force coefficient C_x are obtained by postprocessing the numerical solutions. The normalized velocity component $\frac{U_{AD}}{U_\infty}$ is then combined with the respective AD loading C_T leading to the power coefficient C_P of the duct-AD model as in Equation (4).

3 | COMPUTATIONAL SETTINGS AND PARAMETERS

A commercial DWT model DonQi® is selected as the reference case. The geometrical parameters of the reference DWT model are taken from the existing studies conducted by the authors.[12,13]

The computational set-up replicates the experiments conducted in the closed-loop open-jet (OJF) wind tunnel facility at the Delft University of Technology (see Figure 2). A 0.002-m-thick AD model with porosity ϕ = 70% is used to mimic the rotor. It results in an equivalent thrust

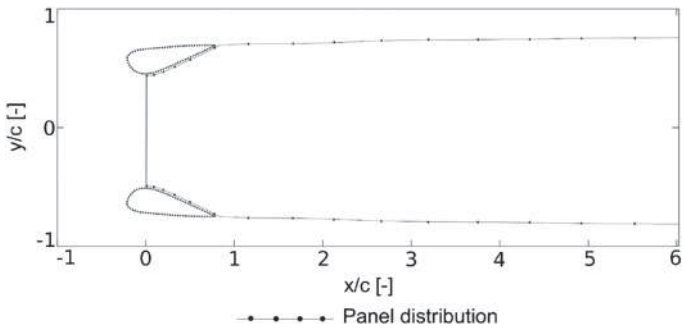

FIGURE 3 Panel distribution along the duct surface and the wake region used for the inviscid panel method calculations

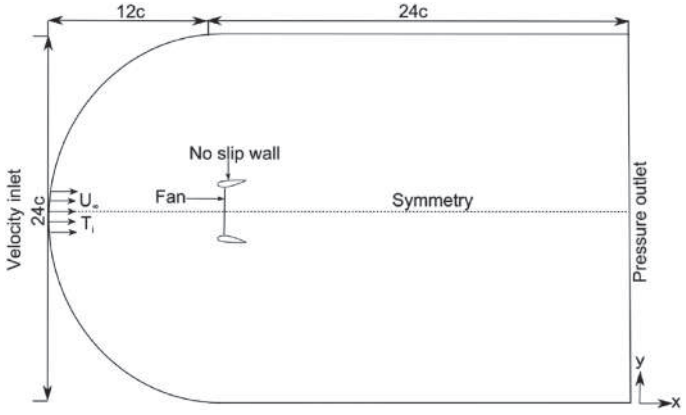

FIGURE 4 Computational domain showing the boundary conditions employed. The length are indicated in terms of duct chord length *c* (representative, not to scale)

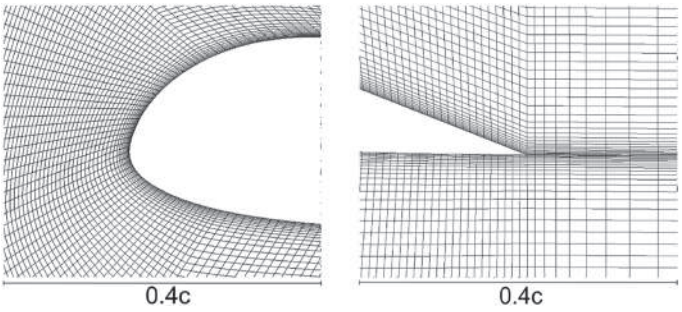

FIGURE 5 Computational grid along the leading and trailing edge of the duct

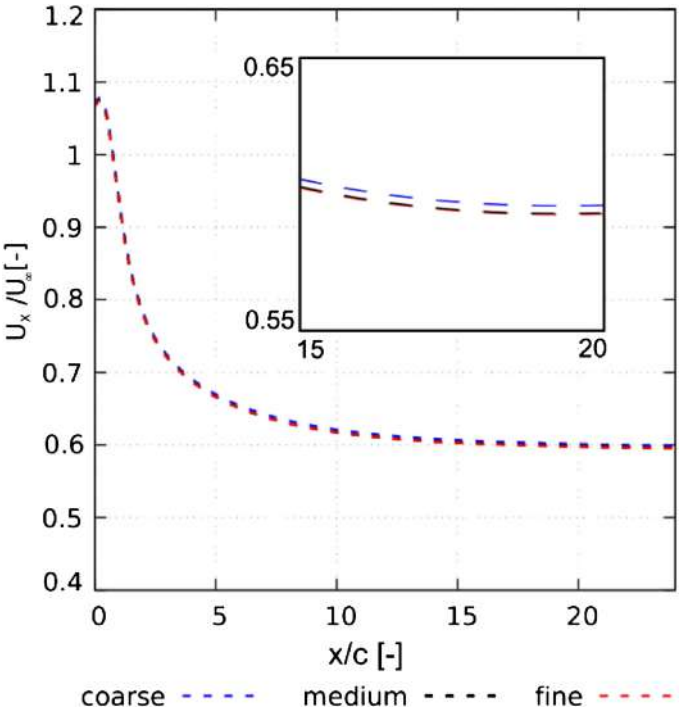

FIGURE 6 Grid independence study showing decay of centre line axial velocity measured across the computational domain [Colour figure can be viewed at wileyonlinelibrary.com]

coefficient, $C_T = 0.65$. Velocimetry measurements are recorded using a constant temperature hot-wire anemometer installed on a traversing system. Surface pressure measurements on the duct were carried out using 52 pressure taps arranged along the chord length. Velocimetry data and pressure measurements are used as reference. During the experiments, the free-stream turbulence intensity, T_i of 0.21%, is measured at the AD location. For all calculations, the lengths are normalized with the duct chord length c. The AD measures $y/c = 1.0$ and located at $x/c = 0.28$. The tip clearance between the AD tip and the duct nozzle surface is 2.0%c. The numerical study is performed at a fixed Re of 4.5×10^5 as in the experiments and various AD loadings $0 \leq C_T \leq 0.89$ are investigated.

In this section, the discretization details of the two computational codes used will be briefly described. For an in-depth description, the reader can refer to de Oliveira et al[14] and Dighe et al.[15]

3.1 | Panel method

A two-dimensional potential flow panel method is used to model the steady isentropic incompressible flow field around the duct-AD model following the work of de Oliviera et al.[14] The governing flow equations are a simple form of the Euler equations. The AD is represented as a nonconservative force term in the vorticity equation. The duct surface is defined using a distribution of vortex panels with the local slope tangential to the duct surface such as to reproduce the desired duct cross-sectional shape; see Figure 3. In essence, a uniform distribution of vorticity on the duct panels is assigned by assuming the Kutta condition. The Kutta condition states that the flow leaves the sharp trailing edge of the duct smoothly. The simplified assumption of uniform vorticity distribution over the panels represents a simplification of real physics and

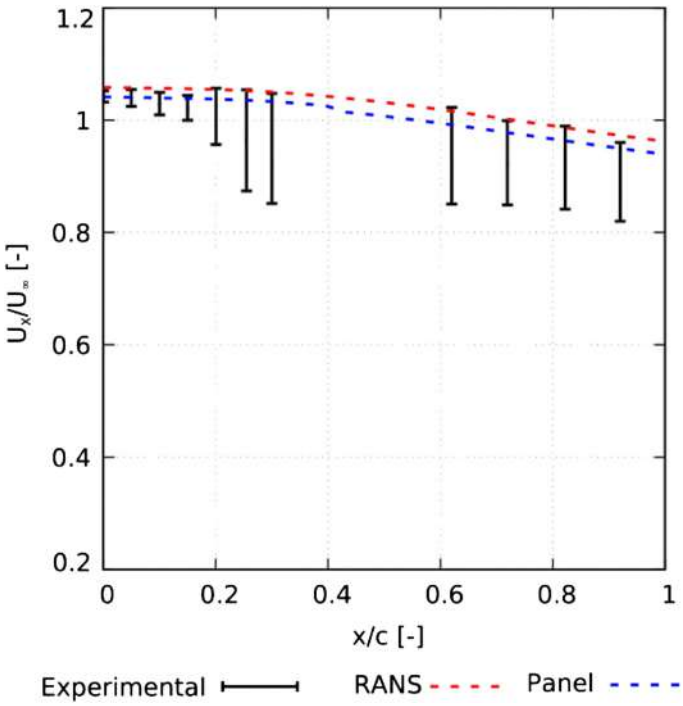

FIGURE 7 Comparison of the numerical results with the experiments. The measurements indicate the axial velocity in the streamwise direction inside of the duct. Error bars indicate the fluctuations in readings from several steady measurements. RANS, Reynold-averaged Navier Stokes [Colour figure can be viewed at wileyonlinelibrary.com]

prevents separation on the duct surface even for larger pressure gradients. The duct surface discretization is based on the constant spacing approach. The streamwise discretization is non-uniform, with initial panel length equal to 1.0%*c* just behind the AD, and increasing gradually in length as the wake expansion settles further downstream. This approach allows to capture the solutions of interest and also to reduce the overall computational costs. Due to the non-linear nature of solutions obtained, the panel method, in any case, should be considered to be a successor of the analytical models used for the analysis of DWT. The panel method is particularly appealing for repeated analysis design arrangements due to its short execution time.

3.2 | RANS method

A commercial CFD tool ANSYS Workbench® has been used for a complete viscous solution of steady incompressible flow around the duct-AD model. The governing flow equations are the Reynolds-averaged Navier Stokes (RANS) equations in planar coordinates. The two-dimensional computational domain is shown in Figure 4, where the distance from the AD location to domain inlet and outlet are 12*c* and 24*c*, respectively. The computational grid consists of quadrilateral cells with maximum y^+ value of 1 on the duct walls (see Figure 5). Boundary conditions are the following: a uniform velocity inlet, zero gauge static pressure outlet, no-slip walls for duct surface, fan boundary condition for AD implementation, and symmetry for centre line axis (see Figure 4). The k-ω SST (shear stress transport) model is used as the turbulence model. Preliminary investigations show good agreement with the experiments.[13] The RANS solution was obtained using the coupled algorithm; it offers robustness and faster convergence for steady state flows as compared to the segregated solution schemes. A least squares cell-based method is used to evaluate the pressure gradient, with pressure and momentum equations solved using a second-order upwind differential scheme. The convergence criteria is set to 10^{-6} for all the residuals. A typical converged RANS solution (single duct-AD configuration) with approximately 0.1 million mesh elements is obtained in roughly 0.5 hour on a multicore work-station desktop computer.

4 | GRID INDEPENDENCE STUDY AND SOLUTION VALIDATION

Solution verification and validation have been performed to ensure the accuracy of the present CFD approach. The results have been published previously.[13,15]

A grid independence analysis for the RANS simulations has been carried out using three grid sizings where the refinement factor in each direction is approximately 1.5. The decay of the axial velocity distribution across the AD in the wake region, from the AD location to the outlet

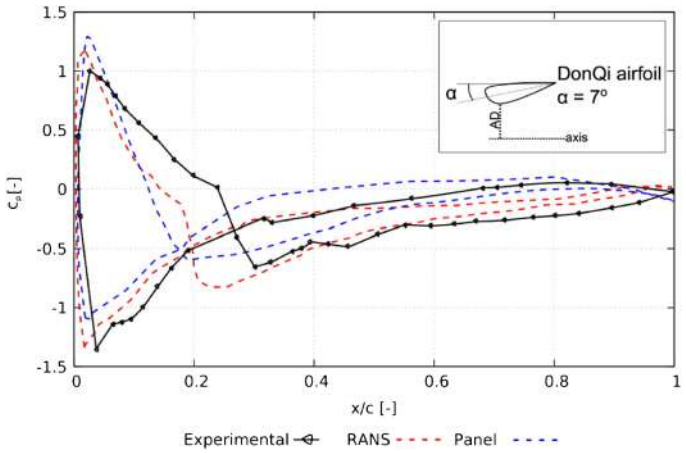

FIGURE 8 Comparison of the numerical surface pressure coefficient c_p with the experiments ($C_T = 0.65$). RANS, Reynold-averaged Navier Stokes [Colour figure can be viewed at wileyonlinelibrary.com]

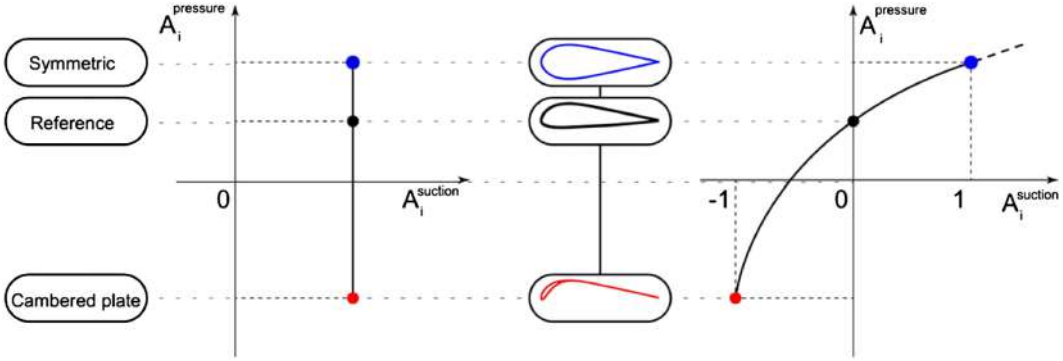

FIGURE 9 Procedure for design of ducted wind turbine (DWT) duct modification in class-shape transformation (CST) parameter space [Colour figure can be viewed at wileyonlinelibrary.com]

of the computational domain, is taken as reference. The results of the grid independence study are shown in Figure 6. The medium refined grid, consisting of approximately 137 600 elements, is selected for the rest of the study.

A validation study have been performed where the CFD results, obtained from the panel method and the RANS method, are compared against the experimental data by Dighe et al.[13] Firstly, the comparison of centre line axial velocity distribution inside of the duct is reported in Figure 7. Error bars represent the fluctuations in readings from several steady measurements. The velocimetry measurements, especially in the region just upstream and just downstream of the AD, fluctuates because of the flow porous medium. The deviation from the experiment is 1.8% to 2.7% and 3.2 to 7.5% for the upstream and downstream locations, respectively. The reason is likely due to the blockage effect of the wind tunnel, which results in an increased velocity decay rate at the measurement locations.[16] Nevertheless, a good agreement is observed between the CFD results and the experiment. Further explanations for the observed deviation and wind tunnel blockage correction methods are comprehensively presented in Dighe et al.[13]

Secondly, Figure 8 shows the comparison of pressure coefficients c_p measured along the surface of the duct. A detailed explanation of the experimental set-up is presented in Dighe et al.[13] The effect of AD is present at the suction side as a pressure jump at AD location. The offset in the locations of the AD between experiment and computations causes the differences in the location of the pressure jump. The AD position during the experimental set-up is at x/c = 0.28 due to the design limitations. Differently, in the computations, the AD is placed at the nozzle plane (x/c = 0.2) in agreement with DWT theory.[2] It is strongly believed that the AD location influences the solution validation; however, the overall computed c_p shows trends in good agreement with the experiment.

5 | DUCT SHAPE PARAMETRIZATION

The duct shapes, in a topological space, represent one-dimensional manifolds whose complete description requires large number of parameters. The manifolds, however, share peculiar features: cross sections always consist of a closed curve forming a smooth leading edge and a cusped

trailing edge. These features are common with airfoil sections, so the design space of all possible duct cross sections can be approximated with airfoil parametrization techniques.

Several methods for parameterizing airfoil shapes have been documented.[17-20] Amongst these, the CST method[19,21] is known to provide nearly complete coverage of the design space.[22] Furthermore, it allows progressive design refinement[23] and does not suffer from surface-waviness issues observed in spline based methods.[24] This section represents the DonQi® reference duct with CST parameters and explains the duct shape modifications in the resulting parametric space. Appendix A includes additional information about the method used for the duct shape parametrization.

The CST representation of the duct describes the relative thickness ($\eta = y/c$) of its sides (suction and pressure) as functions of chord-wise distance ($\xi = x/c$) that depend on $i = 0 \dots M$ shape parameters ($A_i^{suction}$ and $A_i^{pressure}$) :

$$\begin{cases} \eta_{(\xi)}^{pressure} = C_{(\xi)} S_{\left(\xi, A_i^{pressure}\right)} \\ \eta_{(\xi)}^{suction} = -C_{(\xi)} S_{\left(\xi, A_i^{suction}\right)} \end{cases} \quad with \quad C_{(\xi)} = (1-\xi)\sqrt{\xi}. \tag{6}$$

Class functions (C) provide basic topological features, viz, round leading edge and cusped trailing edge, while shape functions (S) represent the specificities of each design.

The parametrization procedure for duct shapes in the current analysis should preserve the following features: leading edge position (which defines the inlet area ratio), trailing edge position (which defines the exit area ratio), and inner side thickness (defines actuator diameter and clearance). This makes it ideal to isolate the effect of camber on the overall performance.[15] The DonQi® duct airfoil (A_i^{ref}) is chosen as the reference shape. In effect of duct shape parametrization, the camber of the DonQi® duct profile is varied by changing its pressure side while leaving its suction side untouched. First, the two extreme variants of the reference shape corresponding to cambered plate profile (A_i^{plt}) and symmetric profile (A_i^{sym}) are defined, see Figure 9.

$$\begin{cases} A_i^{plt,suction} = A_i^{ref,suction} & i = 0 \dots M \\ A_i^{plt,pressure} = -A_i^{ref,suction} & i = 1 \dots M \\ A_i^{plt,pressure} = A_i^{ref,pressure} & i = 0 \end{cases} \qquad \begin{cases} A_i^{sym,suction} = A_i^{ref,suction} & i = 0 \dots M \\ A_i^{sym,pressure} = A_i^{ref,suction} & i = 0 \dots M. \end{cases}$$

The second step consists in obtaining shape parameters for the modified duct profiles (A_i^{mod}) by interpolating between design variants. This is achieved with a quadratic interpolant of a single variable (γ):

$$A_i^{mod} = a_i\gamma^2 + b_i\gamma + c_i \qquad \begin{cases} a_i = \frac{1}{2}\left(A_i^{sym} + A_i^{plt}\right) - A_i^{ref} \\ b_i = \frac{1}{2}\left(A_i^{sym,} - A_i^{plt}\right). \\ c_i = A_i^{ref} \end{cases} \tag{7}$$

The reference DonQi® duct is recovered by setting $\gamma = 0$, while values of $\gamma = 1$ and $\gamma = -1$ produce symmetric and thin plate variants, respectively. Equation (7) provides parameters for any design with γ greater than −1, and duct profile coordinates can be reconstructed from parameters with Equation (6).

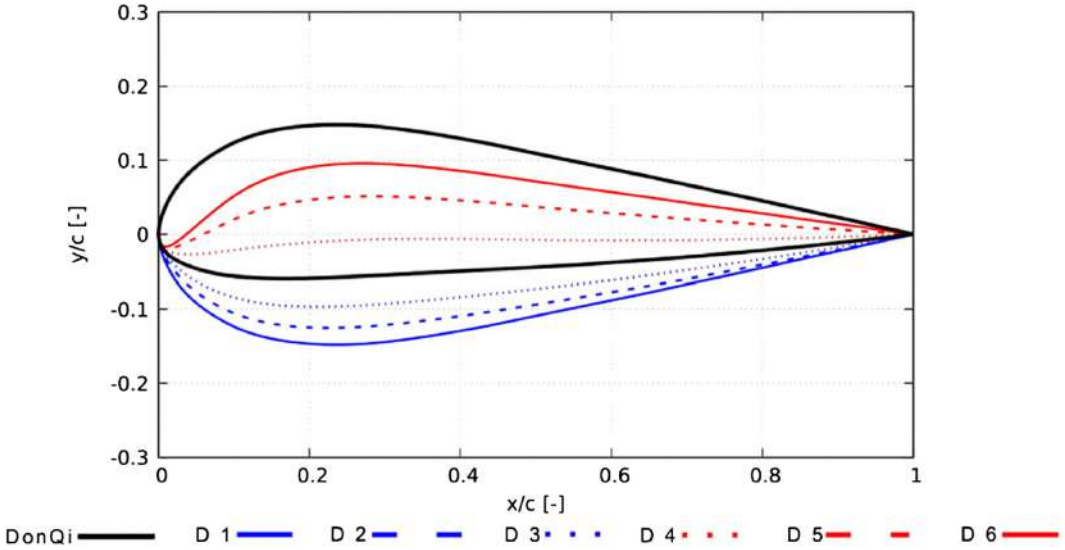

FIGURE 10 Duct profiles used in the numerical study [Colour figure can be viewed at wileyonlinelibrary.com]

6 | RESULTS AND DISCUSSION

This section provides an extensive analysis of the effects of the duct shape on duct force coefficient, see subsection 6.1, and power coefficient, see subsection 6.2. To this aim, seven duct geometries, shown in Figure 10, are adopted. Finally, some insights on the changes occurring to the performance coefficients are obtained through a detailed flow analysis in subsection 6.3.

6.1 | Duct force coefficient

Figures 11 and 12 illustrate the correlation between the duct thrust force coefficient C_x and the AD loading coefficient C_T obtained using the panel and RANS methods, respectively. In general, for lower AD loadings ($C_T \leq 0.6$), the C_x value increases with the increasing C_T. Subsequently, a local C_x maximum for the individual duct airfoils appear. The value of C_x decreases for C_T beyond the local maxima. Furthermore, the magnitude of C_x increases with the duct cross-sectional camber. A good agreement is achieved between the panel and the RANS solutions, with two noticeable exceptions. Firstly, the magnitude of C_x calculated using the panel method is lower than the one calculated with the RANS method across the entire C_T range. Secondly, unlike the panel method solutions, the trend lines for duct airfoils *D*4, *D*5, and *D*6 obtained using the RANS method intersect at higher AD loadings ($C_T \geq 0.6$). In fact, the value of the local maxima attained for duct *D*6 using RANS calculations is lower than the one attained for duct *D*5. The main cause of the differences in the two numerical solutions is the viscous interactions between the duct surface and the AD accounted by RANS solutions only. To this aim, some physical insights on the local flow changes due to the duct camber will be discussed in subsection 6.3. Nevertheless, the comparison of the C_x predictions by both the computational methods indicate that the non-linear mutual interaction between the duct and the AD is taken into account.

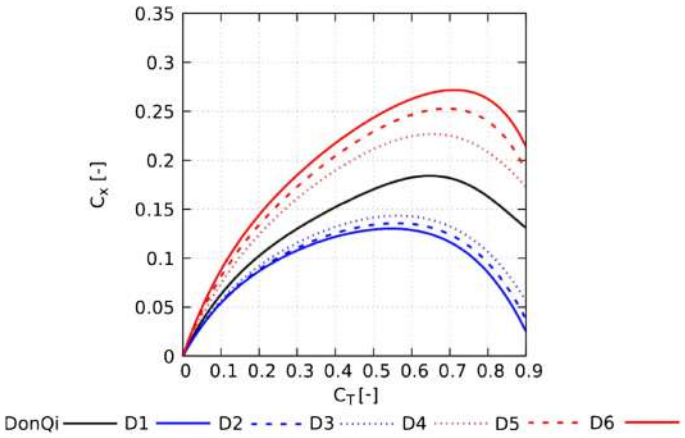

FIGURE 11 Effect of variable actuator disc (AD) loading on duct thrust force coefficient using panel solution [Colour figure can be viewed at wileyonlinelibrary.com]

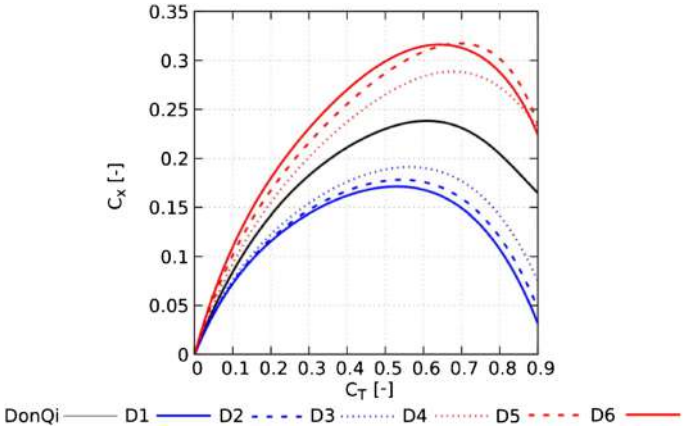

FIGURE 12 Effect of variable actuator disc (AD) loading on duct thrust force coefficient using disc Reynold-averaged Navier Stokes (RANS) solution [Colour figure can be viewed at wileyonlinelibrary.com]

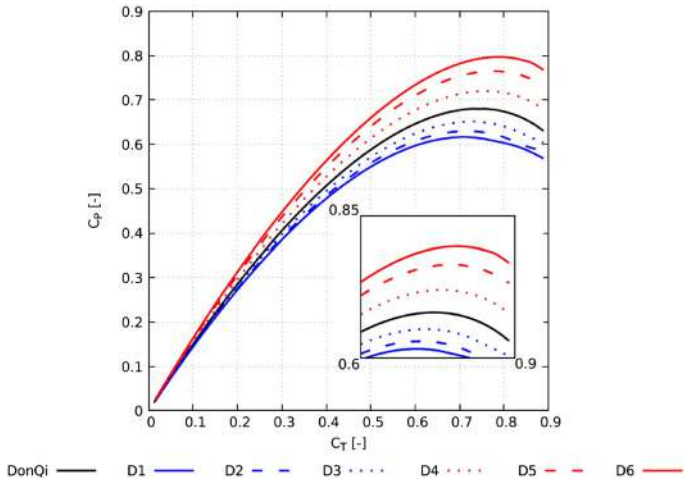

FIGURE 13 Effect of variable actuator disc (AD) loading on power coefficient using panel solution [Colour figure can be viewed at wileyonlinelibrary.com]

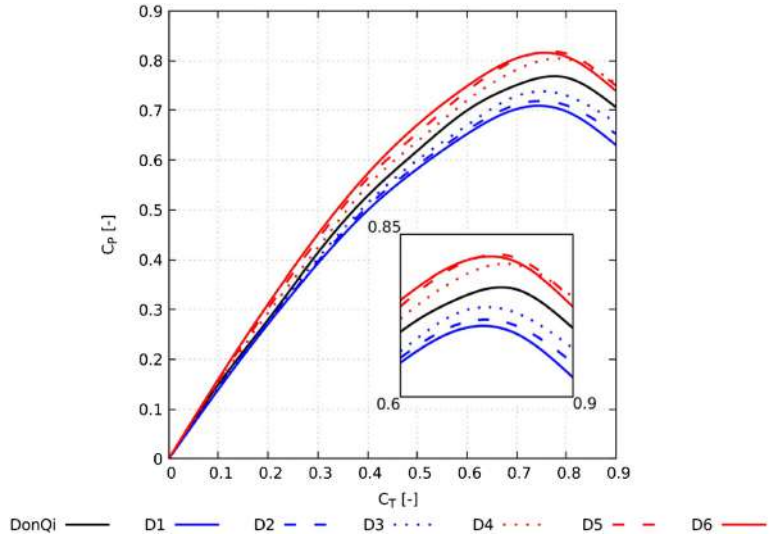

FIGURE 14 Effect of variable actuator disc (AD) loading on power coefficient using Reynold-averaged Navier Stokes (RANS) solution [Colour figure can be viewed at wileyonlinelibrary.com]

6.2 | Power coefficient

Figures 13 and 14 represent the power coefficients C_P, using the panel and RANS solutions, respectively, as a function of variable AD loading C_T. By analogy, the C_P trend appears as a characteristic corollary of the duct force coefficient C_x. The larger the C_x, the higher the C_P reached, and vice versa. Similar to C_x solutions, the C_P trend lines for duct airfoils *D*4, *D*5, and *D*6 obtained using the RANS method begin to intersect at higher AD loadings ($C_T \geq 0.6$). In the absence of viscous mutual interaction, as in the panel solutions, the magnitude of C_x and ultimately the C_P increase with the duct camber. Contrarily, for the RANS solution, the effect of camber on the C_P displays an upper limit. Then, the maximum $C_P \approx 0.82$ is obtained for *D*5 for $C_T \approx 0.75$. Moreover, present results show that the maximum C_P is obtained for a C_T value, which is lower than 8/9, unlike the AMT.[1]

6.3 | Flow field analysis

In order to highlight the effects of the duct shape and the viscous interactions onto the performance coefficients of the duct-AD model, shown in subsections 6.1 and 6.2, a flow field analysis using RANS solutions is carried out. Velocity contours coloured with normalized free stream velocity $\frac{U_x}{U_\infty}$ are shown in Figure 15. Contours are plotted on a plane close to the surface of the duct thus allowing a better interpretation of the flow field associated with duct-AD interactions. In this study, duct airfoils *D*4, *D*5, and *D*6 for $C_T = 0.6, 0.7, 0.8$, and 0.9 are considered to explain the intersecting region in the performance trend lines, as in Figures 12 and 14. It is convenient to start with duct profile *D*4 as a function of C_T, more precisely observing from top to bottom. The velocity contours show that, with the increasing value of C_T, the leading edge stagnation point traverses further up along the suction side of the duct. Consequently, the magnitude of velocity at the suction side of the duct decreases, and the magnitude of velocity on the pressure side of the duct starts to increase significantly. This phenomenon, occurring at the surface of the duct,

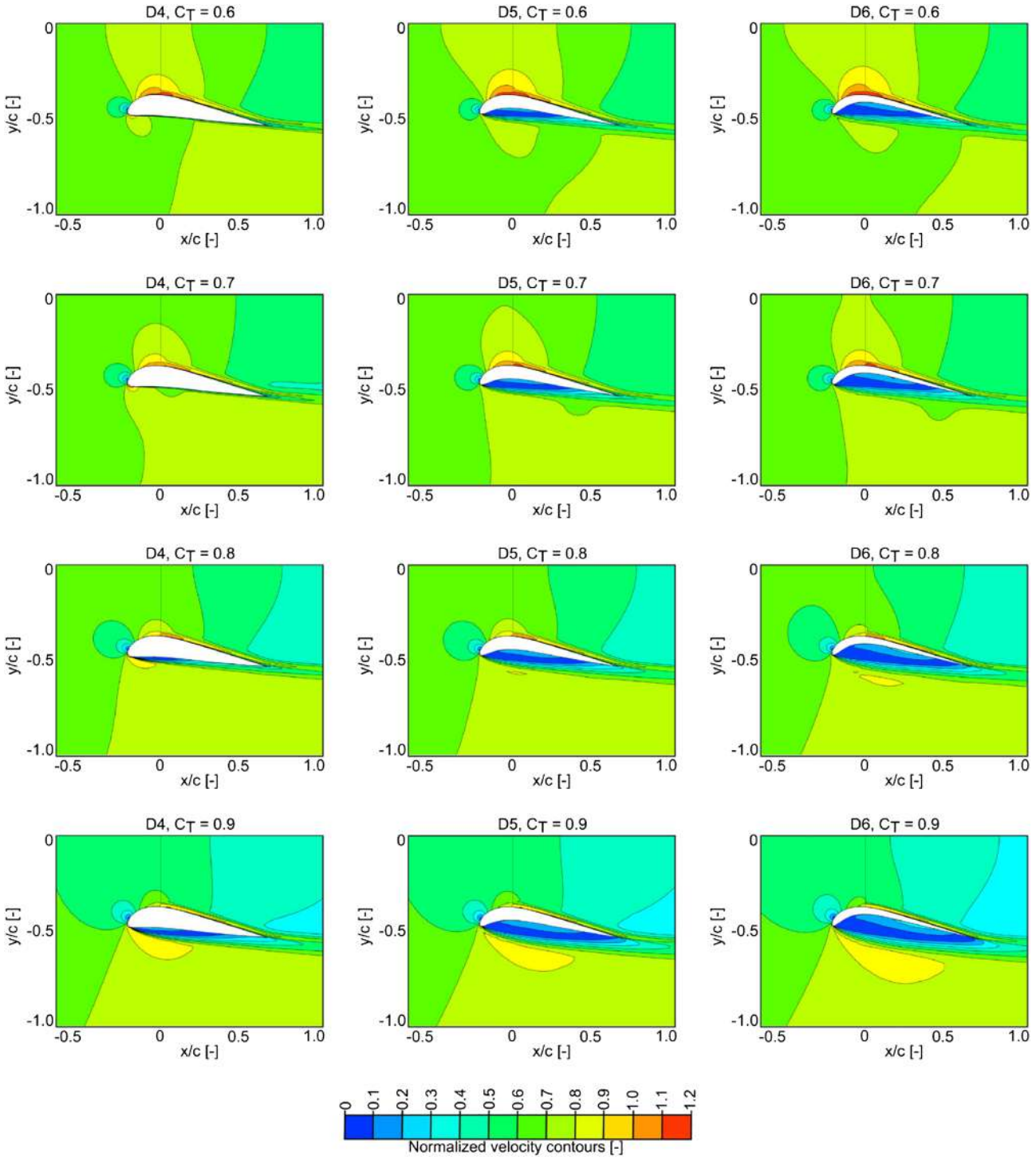

FIGURE 15 Velocity contours coloured with normalized streamwise velocity. The results are depicted for ducts *D*4, *D*5, and *D*6 (left to right) bearing $C_T = 0.6$, 0.7, 0.8, and 0.9 (top to bottom) [Colour figure can be viewed at wileyonlinelibrary.com]

determines the sudden reduction of C_x at high values of C_T as in Figures 11 and 12. Furthermore, from Equation (4), if $\frac{U_{AD}}{U_\infty}$ decreases quickly, C_P also falls for high values of C_T. The above interpretation of flow phenomenon occurring along the duct surface, ultimately governing the global performance of the duct-AD model, also apply to ducts *D*5 and *D*6.

Another very important phenomenon, which also affects the global performance of the duct-AD model, are the viscous effects creating recirculation region along the pressure side of the duct, especially for the highly cambered duct profile. Obviously, the viscous effects exists for RANS calculations only, thus witnessing the intersection of performance trend lines as in Figures 12 and 14. At high values of C_T, the recirculation region traverses from the pressure side of the duct to the suction side of the duct. Evidences of this are witnessed through velocity contours of *D*5 and *D*6, which exhibits flow separation along the trailing edge suction side of the duct for C_T = 0.9 and 0.8, respectively.

The onset of suction-side flow separation, which is earlier for duct *D6* than *D5*, reduces the C_x and ultimately the C_P of the prescribed duct-AD configuration.

7 | CONCLUSION

The investigation presented in this paper focused towards aerodynamic performance improvement of ducted wind turbines using a simplified duct-AD model. To this aim, numerical calculations using panel method and RANS method are performed. A commercial DWT model DonQi® is used as the reference case. Unlike the AMT, the two numerical approaches fully takes into account the non-linear mutual interactions between the duct and the AD. To validate the numerical methods, emphasis has been given to the comparison of numerical results with the experiments. In order to deepen the design principles of DWT, the effects of the duct shape onto the global performance are investigated. An improved duct shape parametrization using CST method is proposed. The study has pointed out that the reference DonQi® duct is not suited for maximum achievable performance. The analysis has shown the possibility to significantly increase the DWT performance by increasing the duct profile camber and a correct choice of rotor loading. In more detail, the overall performance improvement directly corresponds to the dimensionless duct thrust force coefficient. To better highlight the differences between the RANS and the panel codes, solutions for C_x and C_P as a function of C_T are shown. The RANS solutions, however, exhibit an upper limit of the camber extent for maximum achievable performance. This phenomenon is characterized by a rapid reduction of C_x and ultimately the C_P, for highly cambered profile. The analysis highlights the limitations of the panel method when applied to highly cambered duct profiles for DWT analysis. A detailed flow analysis using RANS method shows that highly cambered duct profiles are prone to boundary layer flow separation, which is considered nonoptimal for the overall performance.

The duct shape parametrization is suitable for ducts of general shape and is freely available on contacting the authors.

ACKNOWLEDGEMENTS

Authors would like to acknowledge Juan Tang for providing the experimental data that have contributed to the part of numerical validation reported in this paper. The research is supported by STW organization (grant number 12728).

CONFLICT OF INTEREST

The authors V.V. Dighe, G. de Oliveira, F. Avallone, and G.J.W. van Bussel declare that they have no conflict of interest.

ORCID

Vinit V. Dighe https://orcid.org/0000-0001-6546-0209

REFERENCES

1. van Bussel GJW. The science of making more torque from wind: diffuser experiments and theory revisited. *J Phys Conf Ser*. 2007;75(1):120-10.
2. Foreman KM, Gilbert B, Oman R. Diffuser augmentation of wind turbines. *Sol Energy*. 1978;20(4):305-311.
3. de Vries O. Fluid dynamic aspects of wind energy conversion. Advisory Group for Aerospace Research and Development Neuilly-Sur-Seine (France); 1979.
4. Igra O. Research and development for shrouded wind turbines. *Energy Convers Manag*. 1981;21(1):13-48.
5. Gilbert BL, Foreman KM. Experiments with a diffuser-augmented model wind turbine. *J Energy Resour Technol*. 1983;105(1):46-53.
6. Abe K, Nishida M, Sakurai A, Ohya Y, Kihara H, Wada E, Sato K. Experimental and numerical investigations of flow fields behind a small wind turbine with a flanged diffuser. *J Wind Eng Ind Aerodyn*. 2005;93(12):951-970.
7. Toshimitsu K, Nishikawa K, Haruki W, Oono S, Takao M, Ohya Y. Piv measurements of flows around the wind turbines with a flanged-diffuser shroud. *J Therm Sci*. 2008;17(4):375-380.
8. Werle MJ, Presz WM. Ducted wind/water turbines and propellers revisited. *J Propul Power*. 2008;24(5):1146-1150.
9. Khamlaj TA, Rumpfkeil MP. Theoretical analysis of shrouded horizontal axis wind turbines. *Energies*. 2017;10(1):38.
10. Bontempo R, Manna M. Performance analysis of open and ducted wind turbines. *Appl Energy*. 2014;136:405-416.
11. Bontempo R, Manna M. Effects of the duct thrust on the performance of ducted wind turbines. *Energy*. 2016;99:274-287.
12. Tang J, Avallone F, Bontempo R, van Bussel GJW, Manna M. Experimental investigation on the effect of the duct geometrical parameters on the performance of a ducted wind turbine. *J Phys Conf Ser*. 2018;1037(2):022-034.
13. Dighe VV, Avallone F, Tang J, van Bussel GJW. Effects of gurney flaps on the performance of diffuser augmented wind turbine. In: 35th Wind Energy Symposium; 2017:1382.
14. de Oliveira G, Pereira RB, Ragni D, Avallone F, van Bussel GJW. How does the presence of a body affect the performance of an actuator disk? *J Phys Conf Ser*. 2016;753(2):022-005.
15. Dighe VV, de Oliveira G, Avallone F, van Bussel GJW. Towards improving the aerodynamic performance of a ducted wind turbine: a numerical study. *J Phys Conf Ser*. 2018;1037(2):022-016.
16. Chen TY, Liou LR. Blockage corrections in wind tunnel tests of small horizontal-axis wind turbines. *Exp Therm Fluid Sci*. 2011;35(3):565-569.
17. Hicks RM, Henne PA. Wing design by numerical optimization. *J Aircr*. 1977;15(7):407-412.
18. Sobieczky H. Parametric airfoils and wings. *Notes Numer Fluid Mech, Vieweg Verlag*. 1988;68:71-88.

19. Kulfan B, Bussoletti J. Fundamental parameteric geometry representations for aircraft component shapes. In: 11th AIAA/ISSMO multidisciplinary analysis and optimization conference; 2006:6948.
20. Xiaoqiang L, Jun H, Lei S, Jing L. An improved geometric parameter airfoil parameterization method. *Aerosp Sci Technol*. 2018;78:241-247.
21. Kulfan BM. A universal parametric geometry representation method—CST. 45th AIAA Aerospace Sciences Meeting and Exhibit; 2007.
22. Masters D, Taylor NJ, Rendall T, Allen C, Poole D. A geometric comparison of aerofoil shape parameterisation methods. *AIAA Journal*. 2017;55:1575-1589.
23. de Oliveira G. Wind turbine airfoils with boundary layer suction, a novel design approach. *Msc Thesis*: Delft University of Technology; 2011.
24. Fuglsang P, Bak C, Gaunaa M, Antoniou I. Design and verification of the riso-b1 airfoil family for wind turbines. *J Sol Energy Eng*. 2004;126:1002-1010.
25. More JJ. The levenberg-marquardt algorithm: implementation and theory. *Springer Lect Notes Math*. 1977;630:105-116.
26. Rotor blades for wind turbines. DNVGL-ST-0376 Standard; 2015.
27. Ernst B, Schmitt H, Seume JR. Effect of geometric uncertainties on the aerodynamic characteristic of offshore wind turbine blades. *J Phys Conf Ser*. 2012;555(012033).

How to cite this article: Dighe VV, de Oliveira G, Avallone F, van Bussel GJW. Characterization of aerodynamic performance of ducted wind turbines: A numerical study. *Wind Energy*. 2019;22:1655–1666. https://doi.org/10.1002/we.2388

APPENDIX A: SHAPE PARAMETRIZATION

Shape parameters for existing duct designs can be obtained by solving a regression problem with duct coordinates $\{\eta_{ref}^{outer}, \eta_{ref}^{inner}\}$. A Nth-order shape function corresponds to the linear combination of a complete Bernstein basis of degree M with $N = M + 1$ shape parameters. Convexity is not established for this problem, so it is useful to start by formulating a linear guess $(A_i^{0,ref})$ of the solution:

$$A_i^{0,ref} \;:\; M_{ij} A_j^{0,ref} = B_i \qquad \text{with} \qquad \begin{cases} M_{ij} = C_{(\xi_j)} s_{(\xi_j)}^{iM} \\ \xi_j = \frac{j}{M} \\ B_i = \left(\eta_{ref}\right)_{\xi=\xi_i} \\ i, j = 1 \ldots M \end{cases} \tag{A1}$$

and then proceed to solve the full non-linear problem with a Levenberg-Marquart algorithm.[25] Solutions $\left(A_i^{ref}\right)$ for each side are obtained separately with a simple least squares norm $(\mathcal{L})$:

$$A^{ref} \;:\; \mathcal{L}_{\left(A_i^{ref}, \eta_{ref}\right)} = \min_{A_i} L_{(A_i, \eta_{ref})} \qquad \text{with} \qquad \mathcal{L}_{(A_i, \eta_{ref})} = \int_0^1 \left(C_{(\xi)} S_{(\xi, A_i)} - \eta_{ref} \right)^2 d\xi. \tag{A2}$$

The problems of Equations (A1) and (A2) are solved to fit coordinates of the DonQi reference duct with 16 parameters per side. The resulting 15th degree polynomials match the reference section with a maximum normal offset smaller than 3×10^{-4} chords, which is well below practical manufacturing tolerances.[26,27]

TABLE A1 Modified camber DWT duct sections used in parametric study

Profile	γ Value	Maximum Thickness (%c)	C_L at $\alpha = 0^o$	Shape
D1	+0.9	29.60%	0.002	
D2	+0.6	27.32%	0.124	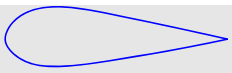
D3	+0.3	24.46%	0.198	
DonQi	0	20.60%	0.312	
D4	−0.3	15.79%	0.524	
D5	−0.6	10.36%	0.703	
D6	−0.8	8.03%	0.809